Cluster-Spin-Glass Magnetic Behavior and Morphology in the Coordination Polymer Alloys FeyCo1–yBTT

Andrew Ritchhart, Zhihengyu Chen, Agnish Behera, Ie-Rang Jeon, Karena W Chapman, Suriyanarayanan Vaikuntanathan, John S Anderson

Cluster-Spin-Glass Magnetic Behavior and Morphology in the Coordination Polymer Alloys $Fe_yCo_{1-y}BTT$

Andrew Ritchhart,[a] Zhihengyu Chen,[b] Agnish Behera,[a] Ie-Rang Jeon,[c] Karena W. Chapman,[b] Suriyanarayanan Vaikuntanathan, [a] and John S. Anderson[a*]

a. Department of Chemistry, University of Chicago, Chicago, Illinois 60637, US

b. Department of Chemistry, Stony Brook University, Stony Brook, New York 11794, US

c. Université de Rennes, Institut des Sciences Chimiques de Rennes, UMR CNRS 6226, 35042 Rennes, France

KEYWORDS: Coordination Polymer, Magnetism, Spin Glass, Alloy, Replica Exchange

ABSTRACT: We report the synthesis of a series of pseudo-1D coordination polymer (CP) materials with the formula $Fe_yCo_{1-y}BTT$ (BTT = 1,3,5-benzenetrithiolate). These materials were structurally characterized by PXRD Rietveld, EXAFS, and PDF analyses, revealing that the CP superstructure enables a continuous and isomorphous alloy between the two homometallic compounds. Lower Fe loadings exhibit emergent spin glass magnetic behavior, such as memory effects and composition-dependent spin glass response time constants ranging from 6.9×10^{-9} s to 1.8×10^{-6} s. These data are consistent with the formation of spin clusters within the lattice. The magnetic behavior in these materials was modeled via replica exchange Monte Carlo simulation which provides a good match for the experimentally measured spin glassing and magnetic phase transitions. These findings underscore how the rigid superstructure of CP and MOF scaffolds can enable the systematic tuning of physical properties such as the spin glass behavior described here.

Introduction

Magnetic spin glass (SG) materials exhibit unusual ground states and represent ideal examples of glassy systems. This makes them an attractive model system for the study of glassiness in fields including physics, economics, biology, and climate sciences.[1–5] In a magnetically glassy system, networks of competing effects, such as simultaneous ferromagnetic and antiferromagnetic coupling modes can lead to multiple "quenched" states which are stable but not necessarily ground states.[6,7] A hallmark of SGs is non-ergodic behavior, where separate states are stable without accessible interconversion, even if they are degenerate. Such SG behavior is believed to be critical to many magnetoresistive and exchange bias mechanisms that are desired for a variety of applications including next generation magnetic data storage and quantum information sciences.[8–14] In these applications the ability to programmably switch between different spin states beyond simple ferromagnetic memory is highly desirable. Canonical SGs include alloys of diamagnetic and spin containing metals such as AuFe[15] and CuMn.[16,17] These systems are structurally amorphous magnetic alloys with SG behavior arising from random magnetic ion distribution in addition to a disordered structure. These properties greatly complicate control over magnetic coupling schema as many possible atomic bonds and orientations exist. Alternatively SG behavior may also arise from geometrical frustration, where patterns such as triangular coupling motifs within ordered materials break the symmetry of otherwise antiferromagnetic ground states.[18]

Topological SGs containing spin centers without structural disorder are less well studied.[19–21] Alternatively to creating "spin jammed" triangular topologies, randomly alloyed metal centers in an ordered lattice in principle would also provide an avenue for tunable SG properties. We rationalized that the rigid periodic superstructure of a CP or metal organic framework (MOF) scaffold might enable systematic spin-doping and control over SG behavior while maintaining a specific topological structure. Furthermore, this regular structure also provides the possibility of a spatially organized and addressable material such as might be required in multi-qubit systems.[22–24] Here we report the synthesis of thiolate-based $Fe_yCo_{1-y}BTT$ (BTT = 1,3,5-benzenetrithiolate) which allows for alloying of Co and Fe centers. We have structurally characterized this set of materials across a broad range of Co/Fe compositions demonstrating that the parent lattice is maintained with alloying. Close examination of the magnetic behavior reveals cluster spin glass (CSG) and memory behavior below a critical alloying limit of approximately 26% Fe, a threshold supported by percolation theory. This limit and the associated magnetic transitions are accurately described and recreated with a statistical mechanical model using differing J_{intra} and J_{inter} coupling strengths simulated via replica exchange Monte Carlo. These findings illustrate how rigid CP superstructures can organize spin-spin interactions to support bulk physical phenomena in a tunable manner and adds to a growing body of literature where paramagnetic CP materials serve as tunable scaffolds for these and related applications.

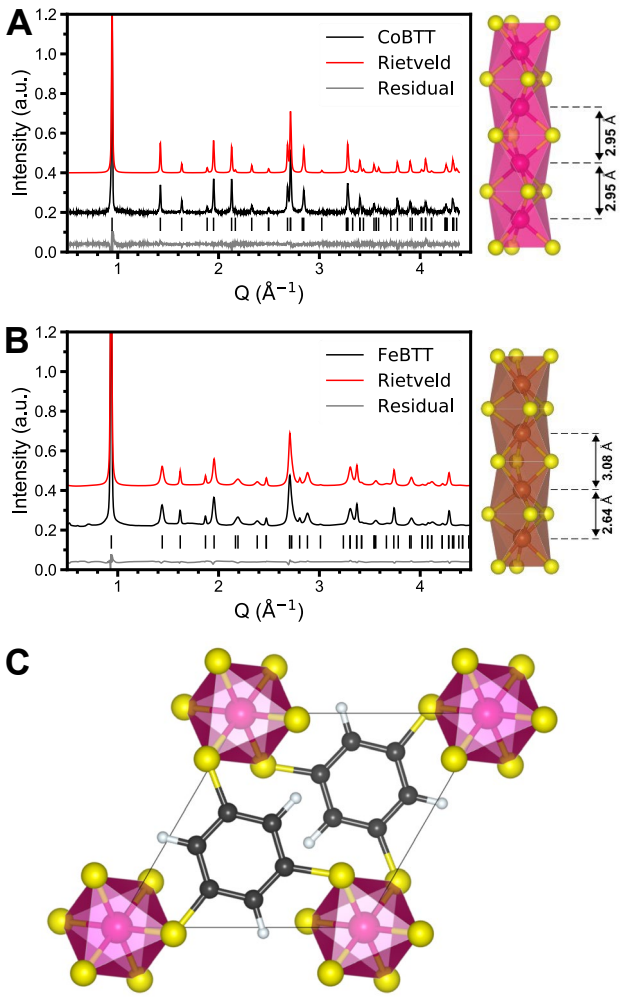

Figure 1. A) Rietveld pattern plotted vs reciprocal vector Q, and diagram of **CoBTT**, a = 7.693 Å, c = 5.904 Å, Co–Co = 2.95 Å, Co–S = 2.23 Å. B) Rietveld pattern and diagram of **FeBTT** showing distinct Fe–Fe distances. a = 7.749 Å, c = 5.718 Å, Fe–Fe = 2.64 Å, 3.08 Å. C) The view along the c-axis of CoBTT displaying the packing of $(CoS_3)_n$ chains linked by BTT ligands.

Results and Discussion

*Structure and Electronic Properties of **CoBTT** and **FeBTT***

The homometallic materials **FeBTT** and **CoBTT** were synthesized using air and water free methods by heating the respective dichloride salts with 1,3,5-benzenetrithiol at 120 °C in DMF overnight. The resulting black powders were purified and found to be nearly isomorphous to the previously reported material CrBTT. The powder X-ray diffraction (PXRD) data for **CoBTT** were indexed with a $P6_3/m$ unit cell with dimensions a = 7.693 Å and c = 5.904 Å. The PXRD data for **FeBTT** were indexed with a P-6 cell of dimensions a = 7.749 Å and c = 5.718 Å (Figure 1). Structural models refined against the data using the Rietveld method, in conjunction with the extended X-ray absorption fine structure (EXAFS) and pair distribution function (PDF) analyses to provide experimental M–S and M–M distances and local structure (Figures S1-7). Both materials form as pseudo-one-dimensional infinite chains of face-sharing MS_6 octahedra, that are linked in the perpendicular plane by BTT ligands. As revealed by the local structure probes EXAFS and PDF, **FeBTT** has lower symmetry from the average structure probed by PXRD. Specifically there are two distinct Fe–Fe distances of 2.64 Å and 3.08 Å which alternate along the c-axis in a long-short pattern. The absence of supercell reflections suggests that the ordering of long-short Fe–Fe distances are not correlated between different chains. Geometry relaxation using DFT also supports this reduced symmetry structure for **FeBTT**, and notably not for **CoBTT** (Figures S8-10). Similar M–S distances of 2.23 Å and 2.29 Å were determined by EXAFS for Co and Fe structures respectively. No difference in the Fe–S length was resolvable for the different long-short pairings which suggests that these are associated with angular deviations from the ideal octahedral geometry.

The empirical formulas of both materials suggest a M^{3+} oxidation state with a d^6 electron configuration for Co and a d^5 electron configuration for Fe. While M^{2+} salts were used in all syntheses, the 3+ oxidation state in the resulting materials suggests an in-situ oxidation. Co^{3+} should populate a low spin state with a covalent radius of 1.26 Å[25] and thus the observed Co–Co distance of 2.95 Å in **CoBTT** implies no metal-metal bond. In contrast, the shorter Fe–Fe distance of 2.64 Å in **FeBTT** is within the sum of the covalent radii for either high or low spin Fe (3.04 Å and 2.64 Å respectively[25]), suggesting some degree of Fe–Fe interaction. As mentioned above, calculated molecular orbitals by DFT support an alternating bonding and nonbonding motif between the short and long Fe pairs with the shorter pair featuring an Fe–Fe σ bond of d_{z^2} character and a node between the longer pair (Figure S10). The driving force for this distortion can be thought of as a disproportionation to satisfy an effective 18 e^- rule as the Fe atoms without this σ interaction would have 17 e^-, and thus form a spin-Peierls distortion.[26,27] Some degree of M–M bonding in **FeBTT** is supported by observations of a significantly lower bandgap and improved bulk conductivity (Figure S11). DFT suggests both materials are semiconducting, and optical bandgap measurements show bandgaps of 1.2 and 0.6 eV for **CoBTT** and **FeBTT** respectively (Figures S12-14). Small semiconducting band gaps have also been found in the BaFeX family of chalcogenides, which adopt a similar quasi-one dimensional MS_6 coordination environment to that observed in **CoBTT** and **FeBTT**.[28–30]

*Alloying of **$Fe_yCo_{1-y}BTT$***

Given the very similar structures of **CoBTT** and **FeBTT** with less than 3% change in the average lattice parameters and M–S bond lengths, we were interested in examining heterometallic materials with mixtures of Fe and Co. Indeed, employing identical synthetic conditions for **CoBTT/FeBTT** with varying ratios of Fe and Co provides alloyed heterometallic materials where the Fe:Co ratio can be controllably tuned by the ratio of starting metal salts. While we previously synthesized CrBTT which is also isostructural with **FeBTT** and **CoBTT**,[31] FeCr alloys were not isolable in practical yields and mixtures of Co and Cr precursors were found to precipitate Co nanoparticles. The composition of **$Fe_yCo_{1-y}BTT$** can be tuned across a broad range from 1 to 56% Fe content, but higher amounts of Fe are not practically accessible due to a consistent decrease in yield with

higher Fe content. This difficulty is plausibly a consequence of the observed Fe–Fe bonding, as the substitution of Co for Fe in the high Fe limit requires breaking Fe–Fe bonds and is thermodynamically disfavored. The alloying concentration can be reliably controlled via the ratio of $CoCl_2$ and $FeCl_2$ used in syntheses using an empirical calibration curve requiring excess $FeCl_2$ (Figure S15). The incorporated ratio of Fe:Co was measured by inductively coupled plasma mass spectrometry (ICP-MS) as well as X-Ray fluorescence (XRF) with both methods agreeing to within 1-2% (Figure S16). No obvious exotic electronic effects from doping were observed in **Fe_yCo_{1-y}BTT**, the conductivity and optical bandgaps of alloys varied linearly, consistent with Vegard's law.[32]

We also investigated the structure of **Fe_yCo_{1-y}BTT** alloys expecting similar linear behavior. PXRD shows that the phase is maintained in the mixed system with linear shifts in the lattice constants as predicted by Vegard's law.[32] However the average structure probed using diffraction cannot reveal the local order of Fe and Co and is insensitive to local changes in symmetry such as the dimerization observed in **FeBTT** or any preferred ordering of metal centers. Understanding of the relative distribution of Fe and Co within the lattice at an atomic level would be highly useful to inform electronic and magnetic observations. We therefore collected PDF from a series of alloy compositions to better understand the metal distribution and atomic level distortions in **Fe_yCo_{1-y}BTT** (Figure 2). The PDF analysis reveals that increasing Fe in the lattice induces significant changes in the local order of **Fe_yCo_{1-y}BTT**, most clearly observed between 2.0 to 3.6 Å in $G(r)$ plotted as the difference from pure **CoBTT** (Figure 2B). A loss of intensity is seen at 2.9 Å which corresponds to a decrease in the mean M–M distance. There is a concomitant increase in two new M–M distances which match well with those in **FeBTT**, ca. 2.7 and 3.1 Å. Similarly, a decrease in the Co–S distance of 2.23 Å is concomitant with an increase of the Fe–S distance of 2.29 Å. Thus, the lower symmetry **FeBTT** model structure proposed from EXAFS and Rietveld data fits the observed changes in the PDF data very well (Figures S1-7). The concerted shift with composition that is observed for the mixed-metal samples by both PDF and PXRD is qualitatively most consistent with formation of a uniform alloy, as mixtures of the parent materials or block copolymers would appear as a superposition rather than a gradual transition.

We then employed non-negative matrix factorization (NMF)[33] as a data extraction technique on the series of PDF measurements with the hope of gaining more insight on the Fe distribution in **Fe_yCo_{1-y}BTT**. NMF is a method of principal component analysis which can decompose convoluted patterns such as those observed for in situ phase transitions and component mixtures.[34,35] Given that this method is a purely mathematical modeling procedure it may be performed *a priori* without imposed chemical or structural model information for unknown components or intermediates. We applied NMF to the experimental PDF data and determined contributions from three principal components: the two known Fe–Fe and Co–Co parent structures, while the third corresponds to unique Fe–Co contributions and related distortions (Figure S17-19). All components have consistent local and long-range order. These results reveal

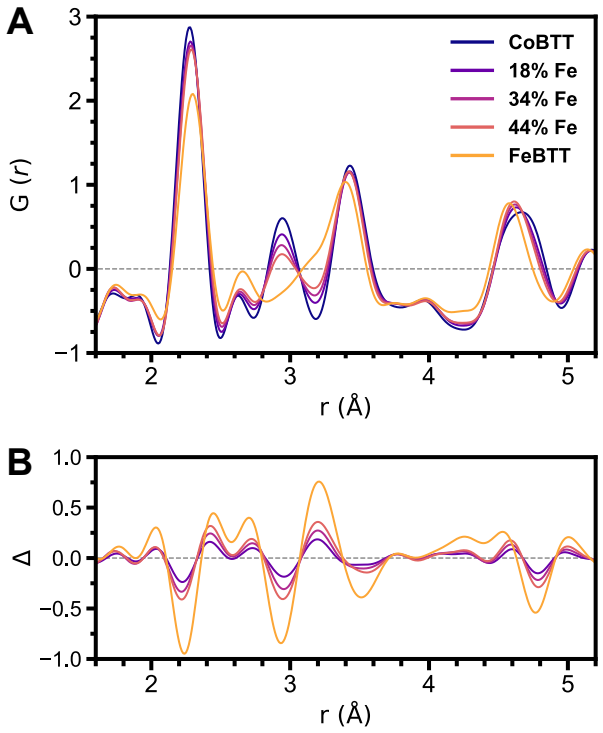

Figure 2. A) Pair Distribution Function (PDF) data for a series of **Fe_yCo_{1-y}BTT** samples collected via synchrotron. B) The difference of observed PDF subtracted with **CoBTT**. Note the large positive residuals ca. 2.7 Å and 3.1 Å which correlate well with the new Fe–Fe distances observed in **FeBTT**.

increasing amounts of both Fe–Fe distances as well as Fe–Co distances in the PDF of the alloys as the composition of Fe is increased, as expected. Once factored, the observed ratio of these extracted principal components can be compared to the statistically expected values for a purely random alloy at a given concentration. This analysis does not provide information on the exact distribution of atoms, but the ratio of components does offer insight on whether Fe centers are more likely to group or cluster as they substitute into the lattice. Comparison of the statistically predicted number of nearest neighbor interactions to the normalized NMF principal components shows fewer Fe–Co interactions than would be expected in a random alloy. We conclude that Fe atoms appear approximately twice as likely to neighbor another Fe atom along the chain than would be expected for a purely random distribution of atoms. Considering that the structure of **FeBTT** suggests that Fe–Fe bonds are formed, some grouping of Fe centers in **Fe_yCo_{1-y}BTT** makes intuitive sense. Nevertheless, only a slight preference for Fe grouping over random chance is still consistent with good mixing on the nanometer scale, and thus the observed smooth transitions which follow Vegard's law.

Magnetic Properties

In order to explore the magnetism of **Fe_yCo_{1-y}BTT** alloys we first examined the susceptibility as χT of the homometallic **CoBTT** and **FeBTT** materials via SQUID magnetometry (Figure 3). Previous magnetic measurements on the analogous CrBTT material were found to be predominantly antiferromagnetic.[31] We predicted CoBTT to be diamagnetic

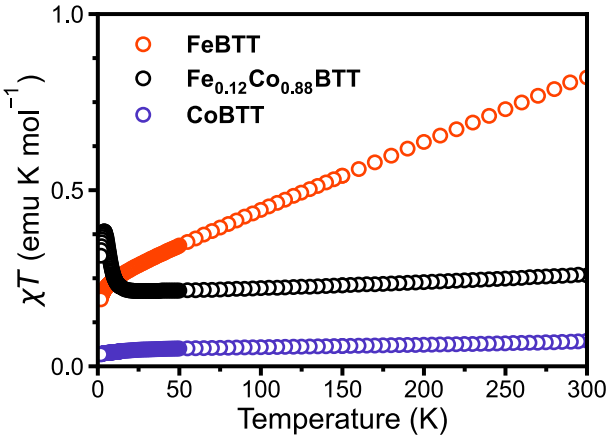

Figure 3. Variable temperature magnetic susceptibility χ multiplied by temperature T data for **FeBTT** (orange), **CoBTT** (Blue), and **$Fe_{0.12}Co_{0.88}$BTT** (Black) as a representative alloy. Values given per mol combined metal (Co + Fe) for this sample.

as it contains d^6 Co^{3+} in a trigonal antiprismatic 2-1-2 split ligand field that should enforce an $S = 0$ ground state as discussed above. DFT calculations also predict a diamagnetic ground state (Figure S9). Variable temperature magnetic susceptibility measurements also report a near zero moment. We posit that any non-zero susceptibility arises from either temperature independent paramagnetism or trace Co^{2+} impurities.[36]

In contrast, the d^5 Fe^{3+} in **FeBTT** has a slightly distorted and low symmetry ligand field as measured by XAS and PDF discussed above. This suggests that many spin states might be possible, $S = 1/2$, $3/2$, or $5/2$. The measured susceptibility of **FeBTT** shows dominant antiferromagnetic character with Curie-Weiss constants of $C = 1.82$ and $\theta_{CW} = -615$ K, corresponding to a $\mu_{eff} = 3.83$ μ_B. This most closely supports an intermediate spin value of $S = 3/2$ ($\mu_{SO,3/2} = 3.87$ μ_B). The intermediate spin value also fits reasonably into the Fisher model[37] of 1D magnetism yielding a fit with $g = 1.94$ and an antiferromagnetic coupling constant of $J = -32$ cm^{-1}, although we note that neither model explicitly captures the alternating of the two Fe–Fe distances (Figures S20-21). Models considering the dimeric nature require a more complex treatment but lead to improved fitting of the magnetic data. Using a Van Vleck Hamiltonian to model the dimeric coupling and treating interdimer coupling as a mean field effect elucidates two AFM coupling values (−14 and −45 cm^{-1}, Figure S22).[38–40] Regardless of the fit used, **FeBTT** appears to be an $S = 3/2$ antiferromagnetic spin chain with slightly nuanced behavior as a result of the alternating dimers, but with no observable ferromagnetism or frustration.

While **FeBTT** displays antiferromagnetic behavior, remarkably different behavior is observed in the susceptibility of mixed **Fe_yCo_{1-y}BTT** alloys with below 30% Fe. In this range we observe a sharp peak in χT below 5 K which depends on composition. The maximum response was observed for y = 0.07 with a peak at 3 K. The moment of this material does not saturate up to 60,000 Oe, displaying a soft ferromagnetic magnetization with relatively low permanence and coercivity of only 200 Oe at 2 K (Figure S24). Under this high field the observed saturation moment is approximately 2.4 μ_B/ Fe. This is lower than expected for an S = 3/2 center but is very close to the pure Fe material (Figure S25). We propose that this suppression arises from competing antiferromagnetic interactions such as interchain effects. We note that competition between multiple interactions, difficulty to saturate, and a large ratio of θ_{CW}/T_f (see below) are all observed characteristics of SG magnetism.[41,42]

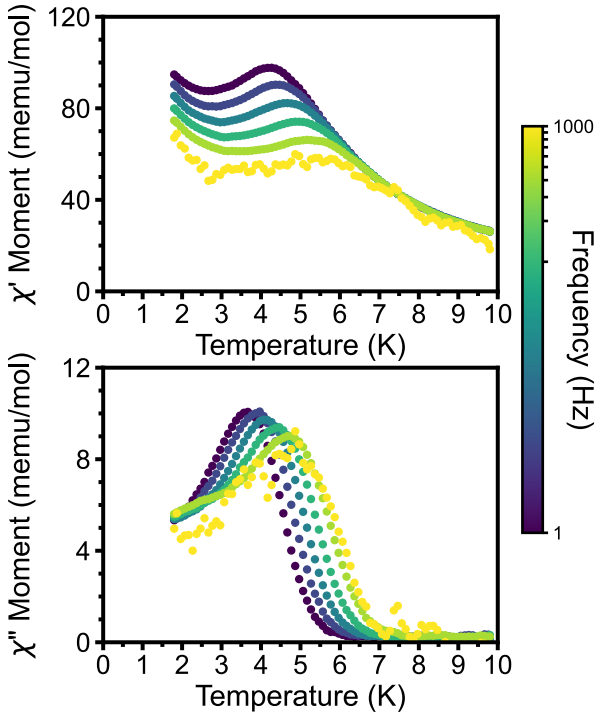

Figure 4. The AC Magnetic susceptibility response of **$Fe_{0.07}Co_{0.93}$BTT** measured from 10 K to 1.8 K at intervals of 0.1 K and at frequencies of 1, 4, 20, 89, 400, and 999 Hz. Top: χ' in-phase component, bottom: χ'' out-of-phase component. AC data for all alloy amounts provided in the SI.

We used AC magnetic susceptibility measurements from 1 to 999 Hz to better understand any SG behavior in **Fe_yCo_{1-y}BTT** (Figure 4). The low temperature peak exhibits both temperature and frequency dependance which is consistent with SG behavior. SG systems are often initially characterized by the Mydosh parameter which quantifies the observed temperature shift per decade frequency. Values below 0.01 are typical for canonical SGs, values from 0.1-0.3 are typical for superparamagnetism, and intermediate values are usually observed for non-canonical, topological, and CSGs.[5,43,44] Alloys of **Fe_yCo_{1-y}BTT** have Mydosh parameters ranging from 0.04-0.09 (Figure S26). These intermediate values are consistent with literature CSGs and trend towards the canonical/dilute SG range with decreasing Fe content.[45] CSGs have been posited in many systems and examined directly via neutron diffraction experiments.[44,46] A CSG model may plausibly arise here from the local AFM Fe–Fe interactions forming randomly distributed Fe clusters, which themselves have secondary or hierarchical coupling modes. Scanning Electron Microscopy (SEM) also reveals that the particle sizes are several microns which is much larger than typically seen for superparamagnets. (Figures S43-46)

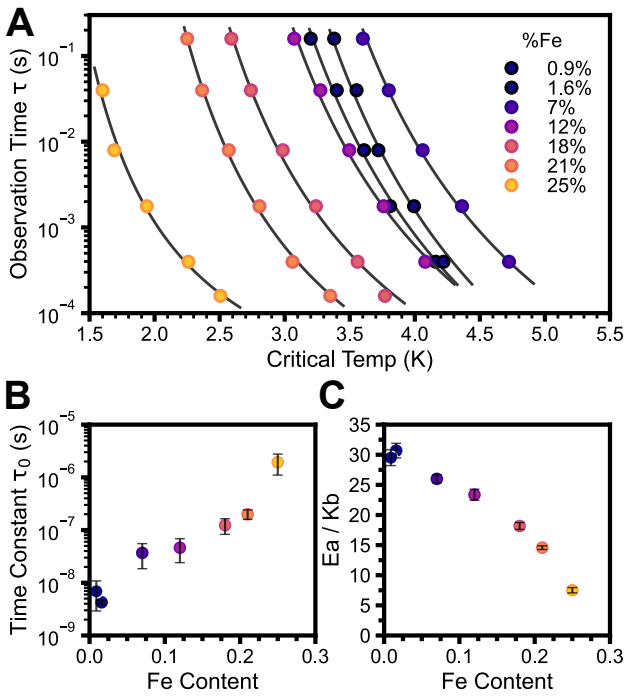

Figure 5. A) Vogel-Fulcher analysis for multiple alloy concentrations. The critical temperatures are plotted for each observation time of the AC susceptibility measurements, $\tau = 1/(2\pi f)$. B) Time constants for each alloy determined from fitting to eq. 2. C) Energy barrier E_a for each alloy determined from fitting.

Measurements of zero-field-cooled (ZFC) splitting at multiple field strengths were fit to the Almeida-Thouless (AT) equation (eq. 1) which semi-empirically describes the SG phase boundary (Figures S27-29 and Table S4). This equation has been derived to associate the field-temperature dependencies of SG freezing temperature T_f as a function of field H, the zero-field freezing temperature T_0, and A which relates to the coupling value J. [47] The exponential term Φ is derived as a constant $\Phi = 3$, but is frequently observed to vary in real systems and has been closely examined as a metric for system anisotropy.[48,49] Fitting the experimental data to eq. 1 yields an exponential term of $\Phi = 5.5$ at high and low Fe concentrations which is in the high anisotropy regime, and much greater than the theoretical value of 3 for a mean field system.[50] Both the hexagonal lattice as well as the random cluster distribution likely contribute to enhanced anisotropy in this system.

$$T_f = T_0\left(1 - AH^{2/\Phi}\right) \quad (1)$$

The explanation for spin glassiness in anisotropic systems has been examined from multiple theoretical perspectives.[43,51,52] In an ordered lattice glassiness typically arises from geometric frustration, either from a combination of local distortions and/or triangular coupling schemes with unstable or degenerate ground states such is in the Kagome lattice.[53] In contrast, glassiness in canonical dilute or amorphous SGs can be theoretically described by competition between FM and AFM couplings which do not necessarily require periodic order. This is rigorously formulated as oscillations in the Ruderman–Kittel–Kasuya–Yosida (RKKY) interaction.[54] While geometric distortion and frustration may arise from lattice strain or the hexagonal structure in **Fe_yCo_{1-y}BTT**, no evidence for magnetic frustration is observed in monometallic **FeBTT** or **CrBTT.** Because these materials have the same triangular motif, this argues against any structurally imposed SG behavior. This leads us to propose that in-plane magnetic coupling is weak in BTT CP systems, or at least too weak to observe frustration arising from the degenerate triangular coupling motif as is seen in some SG systems. Further, the experimental ratio of E_a/T_0 found is approximately 0.1 (see below), which is weaker than typically seen in other geometrically frustrated cases.[55,56]

We measured the AC susceptibility over a range of **Fe_yCo_{1-y}BTT** alloys to further examine cluster domain effects and compositional dependence (Figure 5). The data were fit to the Vogel-Fulcher model (eq. 2) which is a semi-empirical model widely used for SGs to extract a relaxation time constant τ_0, critical temperature T_0, and energy barrier per spin E_a from the frequency dependent glassing temperature T_f for an AC measurement period τ. The data were also fit to the power law as an alternative dynamic scaling relationship (Figure S30 and Table S5). While both relationships are commonly reported together it has been suggested that VF may be superior for larger dynamic ranges such as we observe in τ_0 here.[57] Notably the time constants at high Fe concentrations are slow for canonical SGs, up to $\tau_0 = 1.9 \times 10^{-6}$ s for y = 25%. However, this value is consistent with the literature range of CSGs.[44,46,58] The observed time constants decrease nearly three orders of magnitude with decreasing Fe content, towards $\tau_0 = 6.9 \times 10^{-9}$ s for y = 0.9 %. This trend is consistent with a transition from a CSG to a dilute SG with decreasing Fe concentration and likely arises from a change in the correlation distance.[59] An increase in E_a over this same range is also consistent with literature differences between CSGs and dilute SGs (Table S6).[60]

$$\tau = \tau_0 \exp\left(\frac{E_a}{k_B(T_f - T_0)}\right) \quad (2)$$

One possible compelling application of SGs are as magnetic memory materials. Some glassy systems can be well described by a hierarchical model of their free energy landscape.[61,62] In this description local, metastable states below the critical glassing temperature T_g become increasingly degenerate as the sample is cooled further. Because an energy barrier exists between sub-hierarchies of these states, however, the system is not free to explore all of the phase space i.e. it is non-ergodic. This behavior can manifest as a memory event; a distinctive signature is observed as the system is warmed and the frozen sub-states collapse back into the broader free energy landscape. We evaluated this memory effect experimentally by a modification of the ZFC-FC procedure. The system is cooled under an applied field of 10,000 Oe at a rate of 0.2 K/min. At 2.5 K the field is removed and the system is held for 1 h, after which the field is turned back on and cooling is resumed. Upon warming a discontinuity should manifest at the temperature where the field was previously turned off and the system was allowed to relax.

We performed this scan with **$Fe_{0.07}Co_{0.93}$BTT** and the magnetic data are shown in Figure 6. Cooling is shown as black circles, with the magnetic field turned off at 2.5 K for one hour before being turned back on (with a partially relaxed *X*) and cooled further. Upon warming (red circles), a notable discontinuity is centered at precisely 2.5 K where the field was removed and the system equilibrated into a localized state. It has also been suggested that this phenomena suggests a CSG as long range cluster to cluster interactions may be required to provide an appropriate hierarchical free energy landscape.[50] Regardless, this magnetic memory effect is direct evidence of glassiness and non-ergodicity in **Fe_yCo_{1-y}BTT**.

Spin-Glass Simulations

The unusual SG behavior in **Fe_yCo_{1-y}BTT** and the tunable nature of this SG system motivated us to develop a theoretical model to explain the SG phase behavior of this system. Generally, modeling such systems in a mean-field framework requires parameterization of the effects of doping and geometry as a distribution of coupling strengths between different spin centers in the system.[63–66] While this can lead to a good phenomenological understanding of the SG behavior of a system at low temperature, coarse graining results in the loss of many essential features such as the ability to resolve correlations which may become important close to phase boundaries. Furthermore, given the heterogenous nature our system, we preferred to study its phase behavior using an explicit lattice-based model.

Our lattice model of this system uses the stacked triangular lattice shown in Figure 1. We assume the coupling strength is relatively high along the z-axis as the atoms are coupled through S-mediated super exchange and direct

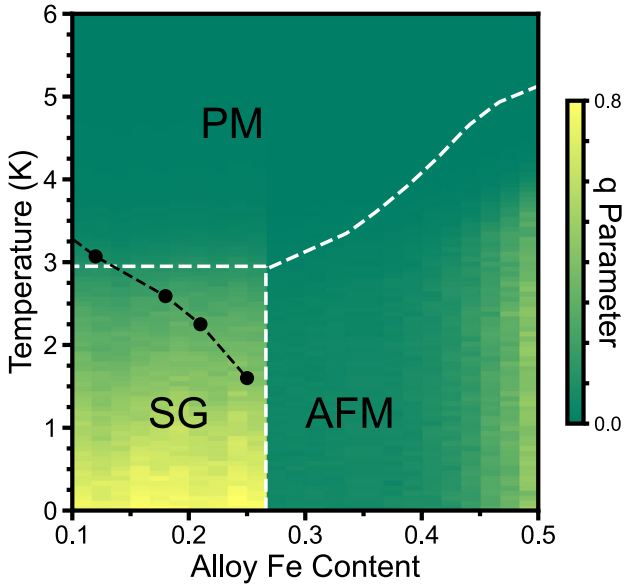

Figure 7. A plot of the glassy q parameter as of Fe_yCo_{1-y}BTT as a function of temperature and composition as determined by Monte-Carlo replica exchange. Plotted in black the experimentally determined glassy freezing temperature of samples determined via AC magnetometry. Phases: PM – Paramagnetic; SG – Spin Glass; AFM – Anti-ferromagnetic.

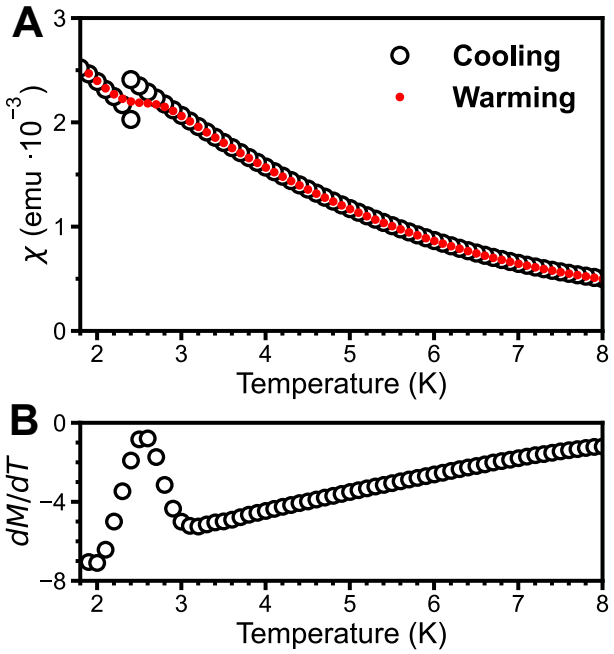

Figure 6. A) Magnetic memory displayed by $Fe_{0.07}Co_{0.93}$BTT under an applied field of 10,000 Oe and a cooling rate of 0.2 K/min. The field was removed for 1 h at 2.5 K during cooling. Open black circles represent the susceptibility while cooling from 8 K, closed red circles are the susceptibility while warming. B) The derivative with respect to temperature of the magnetization while warming displaying a feature at exactly 2.5 K.

Fe–Fe bonds. Along the z-axis we allow for both antiferromagnetic nearest-neighbor and ferromagnetic next-nearest-neighbor interactions. In contrast, we assume weakly ferromagnetic coupling in the xy plane where the spin centers are spaced out by the organic linkers. This assumption is because coupling through the greater distance and through multiple aromatic bonds must be comparatively weaker than exchange along the columns. Coupling to any Co atom is assumed to be zero. From geometrical arguments, for a hexagonal lattice, the site-percolation threshold of Fe concentration is statistically predicted to be around 0.26.[67,68] In effect this is the upper limit before discrete clusters of Fe begin to fuse into extended networks. We ran Replica Exchange Monte Carlo simulations on this model system[69] and obtain a phase diagram that is shown in Figure 7. The two order parameters that we consider are the spin-glass order parameter (q) and the staggered magnetization (Figures S47-48).[70]

Our model predicts a SG region below the critical threshold of 26% Fe at sufficiently cold temperatures. As the amount of Fe increases beyond this point antiferromagnetic behavior dominates, consistent with experimental results. At low Fe loadings, but higher temperatures, a paramagnetic region is predicted. Importantly, our model supports the presence of a SG phase for this topology and the coupling modes described. We have plotted the experimental glass freezing temperature as black points in Figure 7. We see that the experimental results map onto the theoretically predicted phase behavior of **Fe_yCo_{1-y}BTT**.

Conclusion

We have synthesized the novel thiolate-based CPs **CoBTT** and **FeBTT** which were found to have diamagnetic and antiferromagnetic behavior respectively. Co and Fe can alloy effectively in these materials, allowing for the formation of the mixed-metal materials **$Fe_yCo_{1-y}BTT$** across a wide range of compositions up to at least 60% Fe. Structural examination of the binary alloy CPs reveals unit cell shifts consistent with Vegard's law. Close examination using beamline PDF techniques reveals preferential Fe dimerization in the monometallic compound and some preference for Fe clustering in the alloyed materials, most likely driven by the formation of formal Fe–Fe bonds. By alloying diamagnetic and paramagnetic spin centers in the regular periodic CP framework SG behavior emerges that is unique from either parent compound. We characterized this behavior using SQUID magnetometry and found it to be consistent with the formation of Fe spin clusters within the diamagnetic lattice. A variety of magnetic observations including the VF, AT, and Mydosh parameters all support the assignment of cluster SG magnetism specifically.

SG materials, particularly molecule-based SG materials as would be found in a CP, are uncommon. This is especially true for thiolate based and/or non-Kagome structures. Our results demonstrate how SG behavior can arise in a topological yet non-geometrically-frustrated lattice by controlled alloying between two different metal centers. Furthermore, we show that the glassing behavior, including memory effects, of this type of CP can be tuned directly through the degree of alloying. Magnetic SG time constants were controllable over nearly three orders of magnitude by varying the alloy composition and by extension Fe cluster morphology. In order to explain both the glassing behavior as well as its compositional dependance we employed statistical mechanical modeling based on replica theory which supports a glassing region at sufficiently low Fe content and temperature. These results show how the regular and rigid frameworks of CPs provide an ideal platform to systematically investigate SG and related physical behavior.

Experimental

Synthesis of 1,3,5-tris(t-butylthio)benzene

The synthesis of BTT was performed using adapted literature methods for thioether formation[71] and deprotection,[72] and is effective towards the bulk synthesis of a variety of aryl thiols. Initially, we generated 1,3,5-tris(*t*-butylthio)benzene, which has been previously reported via a different synthetic route.[73] A 500 mL round bottomed flask under N_2 atmosphere is charged with 7.2 g (180 mmol, 6 eq) NaH (60%) which is washed and decanted twice with 50 mL of petroleum ether. The flask is charged with 100 mL of dried and degassed DMF. The flask is placed in an ice bath and equipped with dropping funnel. The dropping funnel is charged with 20.2 mL (16.2g, 180 mmol, 6 eq) of t-butyl thiol which is added over the course of 30 m. Some bubbling is seen and a faint yellow color develops. Under counterflow of N_2 9.5 g (30 mmol, 1 eq) of 1,3,5-tribromobenzene is added and the flask is placed in a 110 °C oil bath for 15 h under N_2 developing a large amount of white precipitate. Once cooled 100 mL water is added to the flask dissolving most of the precipitate and the mixture is transferred to a separation funnel. Three extractions are performed with 75 mL diethyl ether. The organic extract is then washed 4 times with 50 mL water. The organic extract is concentrated in vacuo and then filtered through a 3 cm silica plug using a 1:1 benzene:hexanes eluent. After drying NMR-pure 1,3,5-tris(*t*-butylthio)benzene is obtained as an off-white powder, 8.2 g, 87%. This isolated powder was characterized by ^{1}H NMR which matched previous literature reports. ^{1}H NMR (400 MHz, C_6D_6) δ 8.05 (s, 3H), 1.18 (s, 27H).

Synthesis of 1,3,5-tris(acetylsulfanyl)benzene

The intermediate 1,3,5-tris-acetylsulfanyl-benzene has also been previously synthesized by a different route.[74] Under N_2 a 500 mL round bottom flask is charged with 8.2 g of 1,3,5-tris-*t*-butylthiobenzene (24 mmol, 1 eq) and 150 mL dry DCM. The flask is cooled in an ice bath and 5.6 mL of acetyl chloride (79 mmol, 3.3 eq) is added. Slowly, 48 mL of 0.1 M $TiCl_4$ in DCM (48 mmol, 2.0 eq) is added developing a deep orange color. The flask is removed from the bath to warm to room temperature and allowed to stir for 2 h. Manual shaking is used to break up precipitate. After stirring 150 mL water is added slowly dissipating most precipitate. The contents are transferred to a separation funnel and the organic layer is extracted followed by two additional extractions with 50 mL DCM. The organic extract is washed with 3 portions of 50 mL water. The organic extract was finally dried with $MgSO_4$, filtered, and dried under vacuum yielding an orange oil of 1,3,5-tris(acetylsulfanyl)benzene, 6.8 g, 95%. This isolated oil was characterized by ^{1}H NMR and used without further purification. ^{1}H NMR (400 MHz, C_6D_6) δ 7.58 (s, 3H), 1.75 (s, 9H).

Synthesis of 1,3,5-benzenetrithiol

1,3,5-benzenetrithiol has also been previously reported via a different route.[73] In a 250 mL round bottom flask under N_2 6.8 g (22 mmol, 1 eq) of 1,3,5-tris(thioacetate)benzene is loaded and dissolved in 100 mL of a 60:40 mixture of DCM and MeOH. To the solution 0.4 mL of concentrated 15 M H_2SO_4 (66 mmol, 3 eq) was slowly added in a dropwise manner. The solution was gently warmed to 35 °C and left to stir for 15 h yielding a cloudy white solution. The flask was dried under vacuum yielding yellow powder which was transferred into the glovebox. The powder can be recrystallized from 1:1 layered hexanes over saturated DCM solution yielding white needles of 1,3,5-benzenetrithiol, 2.4 g, 60%. These isolated needles were characterized by ^{1}H NMR which matched previous literature reports. ^{1}H NMR (400 MHz, C_6D_6): δ 6.45 (s, 3H), 2.80 (s, 3H).

Syntheses of CoBTT and FeBTT

The syntheses of both CoBTT and FeBTT are nearly identical employing different anhydrous metal salt precursors. In a nitrogen glovebox a thick walled 24 mL glass vial in a glovebox is loaded with 19 mg (0.15 mmol, 1 eq) of $CoCl_2$ (or $FeCl_2$) and 32 mg of BTT (0.19 mmol, 1.25 eq). These are dissolved in 3 mL of DMF and the vial is sealed and placed into a 120 °C aluminum block for 16 h. Slightly improved yields were observed by adding 5 eq of Et_3N to FeBTT syntheses prior to heating. After cooling, black precipitate is

isolated via repeated centrifugation and washing three times with 1.5 mL portions of DMF, followed by 2 portions of 1.5 mL MeCN, and 2 portions of 1.5 mL THF. The final powders are dried under vacuum and stored under inert atmosphere. Although stored and handled under inert atmosphere these products were not observed to be air sensitive. CoBTT 18 mg, 82%. FeBTT 8 mg, 37%.

Synthesis of $Co_yFe_{1-y}BTT$

Alloys of Co and Fe were made in an identical way using stock solutions in DMF of $FeCl_2$ and $CoCl_2$ measured via micropipette rather than dry measurements. The total molar amount of metal was held constant at 0.15 mmol while adjusting the ratio of Co:Fe and the solution volume was held constant at 3 mL DMF as well. The ratios of metals used in synthesis require an excess of Fe over the observed ratio (see Figure S18). 7-20 mg, 32-85%, decreasing yield with increasing Fe.

ASSOCIATED CONTENT

Additional methods and data including computational details, XAS data, crystallographic, and spectroscopic data are available in the supplementary information.

ACCESSION CODES

CCDC 2249612 and CCDC 2249613 contain the supplementary crystallographic data for CoBTT and FeBTT respectively. These data can be obtained free of charge via www.ccdc.cam.ac.uk/data_request/cif, or by emailing data_request@ccdc.cam.ac.uk, or by contacting The Cambridge Crystallographic Data Centre, 12 Union Road, Cambridge CB2 1EZ, UK; fax: +441,223 336,033.

AUTHOR INFORMATION

Corresponding Author

* John S. Anderson

Author Contributions

The manuscript was written through contributions of all authors.

ACKNOWLEDGMENT

This research was supported by the U.S. National Science Foundation (DMR-2002367), the Catalyst Design for Decarbonization Center (DE-SC0023383), and by a FACCTS grant through the France Chicago Center. JSA gratefully acknowledges support from a Dreyfus Teacher-Scholar award (TC-21-064). This work made use of the shared facilities at the University of Chicago Materials Research Science and Engineering Center, supported by the National Science Foundation under award number DMR-2011854. MRCAT operations are supported by the Department of Energy and the MRCAT member institutions. This research used resources of the Advanced Photon Source beamline 11-ID-B and 10-BM, a Department of Energy (DOE) Office of Science User Facility operated for the DOE Office of Science by Argonne National Laboratory under Contract No. DE-AC02-06CH11357. S.V. acknowledges support from the U.S. National Science Foundation under Grant No. DMR-1848306. I. J. acknowledges support from French National Research Agency Grants, ANR-22-CE07-0050. We would also like to thank Alex Anferov for his expertise and help in SEM acquisition.

ABBREVIATIONS

SG Spin Glass; CSG Cluster Spin Glass; CP Coordination Polymer; BTT 1,3,5-benzenetrithiolate; PDF Pair Distribution Function; EXAFS Extended X-ray Absorption Fine Structure; PXRD Powder X-ray Diffraction; SQUID Superconducting Quantum Interference Device

REFERENCES

(1) Hegerl, G.; Zwiers, F. Use of Models in Detection and Attribution of Climate Change. *WIREs Climate Change* **2011**, *2* (4), 570–591.

(2) Sánchez-Granero, M. A.; Trinidad-Segovia, J. E.; Clara-Rahola, J.; Puertas, A. M.; De Las Nieves, F. J. A Model for Foreign Exchange Markets Based on Glassy Brownian Systems. *PLoS One* **2017**, *12* (12), e0188814.

(3) Teeter, M. M.; Yamano, A.; Stec, B.; Mohanty, U. On the Nature of a Glassy State of Matter in a Hydrated Protein: Relation to Protein Function. *Proc. Natl. Acad. Sci. U.S.A.* **2001**, *98* (20), 11242–11247.

(4) Binder, K.; Young, A. P. Spin Glasses: Experimental Facts, Theoretical Concepts, and Open Questions. *Rev. Mod. Phys.* **1986**, *58* (4), 801–976.

(5) Mydosh, J. A. Spin Glasses: Redux: An Updated Experimental/Materials Survey. *Rep. Prog. Phys.* **2015**, *78* (5), 052501.

(6) Alexandrov, D. V.; Zubarev, A. Yu. Heterogeneous Materials: Metastable and Non-Ergodic Internal Structures. *Philos. Trans. R. Soc. A* **2019**, *377* (2143), 20180353.

(7) Çakır, Ö.; Cugini, F.; Solzi, M.; Priolkar, K.; Acet, M.; Farle, M. Dynamics of Nonergodic Ferromagnetic/Antiferromagnetic Ordering and Magnetocalorics in Antiperovskite Mn_3SnC. *Phys. Rev. B* **2017**, *96* (1), 014436.

(8) Niimi, Y.; Kimata, M.; Omori, Y.; Gu, B.; Ziman, T.; Maekawa, S.; Fert, A.; Otani, Y. Strong Suppression of the Spin Hall Effect in the Spin Glass State. *Phys. Rev. Lett.* **2015**, *115* (19), 196602.

(9) Murphy, R. A.; Darago, L. E.; Ziebel, M. E.; Peterson, E. A.; Zaia, E. W.; Mara, M. W.; Lussier, D.; Velasquez, E. O.; Shuh, D. K.; Urban, J. J.; Neaton, J. B.; Long, J. R. Exchange Bias in a Layered Metal–Organic Topological Spin Glass. *ACS Cent. Sci.* **2021**, *7* (8), 1317–1326.

(10) Nashaat, A. M.; Abu El-Fadl, A.; Nakamura, H.; Kassem, M. A. Glassy Magnetic Freezing and Exchange Bias Effect in $NiCo_2O_4$/(Co-Ni)O Nanoparticles Composite. *J. Magn. Magn. Mater.* **2023**, *567*, 170366.

(11) Schlenker, C.; Parkin, S. S. P.; Scott, J. C.; Howard, K. Magnetic Disorder in the Exchange Bias Bilayered FeNi-FeMn System. *J. Magn. Magn. Mater.* **1986**, *54–57*, 801–802.

(12) Tejada, J.; Chudnovsky, E. M.; Barco, E. del; Hernandez, J. M.; Spiller, T. P. Magnetic Qubits as Hardware for Quantum Computers. *Nanotechnology* **2001**, *12* (2), 181–186.

(13) Blachowicz, T.; Ehrmann, A. Exchange Bias in Thin Films—An Update. *Coatings* **2021**, *11* (2), 122.

(14) Puebla, J.; Kim, J.; Kondou, K.; Otani, Y. Spintronic Devices for Energy-Efficient Data Storage and Energy Harvesting. *Commun Mater* **2020**, *1* (1), 1–9.

(15) Cannella, V.; Mydosh, J. A. Magnetic Ordering in Gold-Iron Alloys. *Phys. Rev. B* **1972**, *6* (11), 4220–4237.

(16) Kouvel, J. S. The Ferromagnetic-Antiferromagnetic Properties of Copper-Manganese and Silver-Manganese Alloys. *J. Phys. Chem. Solids* **1961**, *21* (1), 57–70.

(17) Monod, P.; Préjean, J. J.; Tissier, B. Magnetic Hysteresis of CuMn in the Spin Glass State. *J. Appl. Phys* **1979**, *50* (B11), 7324–7329.

(18) Oberberg, M.; Berger, B.; Buschheuer, M.; Engel, D.; Wölfel, C.; Eremin, D.; Lunze, J.; Brinkmann, R. P.; Awakowicz, P.; Schulze, J. The Magnetic Asymmetry Effect in Geometrically Asymmetric Capacitively Coupled Radio Frequency Discharges Operated in Ar/O_2. *Plasma Sources Sci. Technol.* **2020**, *29* (7), 075013.

(19) Chandra, P.; Coleman, P.; Ritchey, I. The Anisotropic Kagome Antiferromagnet: A Topological Spin Glass? *J. Phys. I France* **1993**, *3* (2), 591–610.

(20) Sen, A.; Moessner, R. Topological Spin Glass in Diluted Spin Ice. *Phys. Rev. Lett.* **2015**, *114* (24), 247207.

(21) Liu, C.-M.; Luo, J.-L.; Zhang, D.-Q.; Wang, N.-L.; Chen, Z.-J.; Zhu, D.-B. Spin Glass Behaviour in a 1D Mixed Molybdenum-Vanadium Heteropolyoxometalate-Bridged Coordination Polymer. *Eur. J. Inorg. Chem.* **2004**, *2004* (24), 4774–4779.

(22) Zadrozny, J. M.; Gallagher, A. T.; Harris, T. D.; Freedman, D. E. A Porous Array of Clock Qubits. *J. Am. Chem. Soc.* **2017**, *139* (20), 7089–7094.

(23) Jazaeri, F.; Beckers, A.; Tajalli, A.; Sallese, J.-M. A Review on Quantum Computing: Qubits, Cryogenic Electronics and Cryogenic MOSFET Physics. arXiv August 7, 2019.

(24) Kjaergaard, M.; Schwartz, M. E.; Braumüller, J.; Krantz, P.; Wang, J. I.-J.; Gustavsson, S.; Oliver, W. D. Superconducting Qubits: Current State of Play. *Annu. Rev. Condens. Matter Phys* **2020**, *11* (1), 369–395.

(25) Cordero, B.; Gómez, V.; Platero-Prats, A. E.; Revés, M.; Echeverría, J.; Cremades, E.; Barragán, F.; Alvarez, S. Covalent Radii Revisited. *Dalton Trans.* **2008**, No. 21, 2832–2838.

(26) Bray, J. W.; Interrante, L. V.; Jacobs, I. S.; Bonner, J. C. The Spin-Peierls Transition. In *Extended Linear Chain Compounds: Volume 3*; Miller, J. S., Ed.; Springer US: Boston, MA, 1983; pp 353–415.

(27) Nishi, M. Evidence of a Spin-Peierls Distortion in the Quasi-One-Dimensional Magnetic Compound $CuGeO_3$. *J. Phys.: Condens. Matter* **1994**, *6* (3), L19.

(28) Takahashi, H.; Sugimoto, A.; Nambu, Y.; Yamauchi, T.; Hirata, Y.; Kawakami, T.; Avdeev, M.; Matsubayashi, K.; Du, F.; Kawashima, C.; Soeda, H.; Nakano, S.; Uwatoko, Y.; Ueda, Y.; Sato, T. J.; Ohgushi, K. Pressure-Induced Superconductivity in the Iron-Based Ladder Material $BaFe_2S_3$. *Nature Mater* **2015**, *14* (10), 1008–1012.

(29) Zhang, Y.; Lin, L.; Zhang, J.-J.; Dagotto, E.; Dong, S. Pressure-Driven Phase Transition from Antiferromagnetic Semiconductor to Nonmagnetic Metal in the Two-Leg Ladders AFe_2X_3 (A=Ba,K; X=S,Se). *Phys. Rev. B* **2017**, *95* (11), 115154.

(30) Zhang, J.; Duan, L.; Wang, Z.; Wang, X.; Zhao, J.; Jin, M.; Li, W.; Zhang, C.; Cao, L.; Deng, Z.; Hu, Z.; Agrestini, S.; Valvidares, M.; Lin, H.-J.; Chen, C.-T.; Zhu, J.; Jin, C. The Synthesis of a Quasi-One-Dimensional Iron-Based Telluride with Antiferromagnetic Chains and a Spin Glass State. *Inorg. Chem.* **2020**, *59* (8), 5377–5385.

(31) Ritchhart, A.; Filatov, A. S.; Jeon, I.-R.; Anderson, J. S. Structure and Magnetic Properties of Pseudo-1D Chromium Thiolate Coordination Polymers. *Inorg. Chem.* **2023**, *62* (6), 2817–2825.

(32) Denton, A. R.; Ashcroft, N. W. Vegard's Law. *Phys. Rev. A* **1991**, *43* (6), 3161–3164.

(33) Liu, C.-H.; Wright, C. J.; Gu, R.; Bandi, S.; Wustrow, A.; Todd, P. K.; O'Nolan, D.; Beauvais, M. L.; Neilson, J. R.; Chupas, P. J.; Chapman, K. W.; Billinge, S. J. L. Validation of Non-Negative Matrix Factorization for Rapid Assessment of Large Sets of Atomic Pair Distribution Function Data. *J. Appl. Crystallogr.* **2021**, *54* (3), 768–775.

(34) Long, C. J.; Bunker, D.; Li, X.; Karen, V. L.; Takeuchi, I. Rapid Identification of Structural Phases in Combinatorial Thin-Film Libraries Using x-Ray Diffraction and Non-Negative Matrix Factorization. *Rev. Sci. Instrum.* **2009**, *80* (10), 103902.

(35) Todd, P. K.; Wustrow, A.; McAuliffe, R. D.; McDermott, M. J.; Tran, G. T.; McBride, B. C.; Boeding, E. D.; O'Nolan, D.; Liu, C.-H.; Dwaraknath, S. S.; Chapman, K. W.; Billinge, S. J. L.; Persson, K. A.; Huq, A.; Veith, G. M.; Neilson, J. R. Defect-Accommodating Intermediates Yield Selective Low-Temperature Synthesis of $YMnO_3$ Polymorphs. *Inorg. Chem.* **2020**, *59* (18), 13639–13650.

(36) Cossee, P. Magnetic Properties of Cobalt in Oxide Lattices. *J. Inorg. Nucl. Chem.* **1958**, *8*, 483–488.

(37) Fisher, M. E. Magnetism in One-Dimensional Systems—The Heisenberg Model for Infinite Spin. *Am. J. Phys.* **1964**, *32* (5), 343–346.

(38) Clérac, R.; Miyasaka, H.; Yamashita, M.; Coulon, C. Evidence for Single-Chain Magnet Behavior in a Mn^{III} –Ni^{II} Chain Designed with High Spin Magnetic Units: A Route to High Temperature Metastable Magnets. *J. Am. Chem. Soc.* **2002**, *124* (43), 12837–12844.

(39) K. S. Murray. Binuclear Oxo-Bridged Iron(III) Complexes. *Coord. Chem. Rev.* **1974**, *12*, 1–35.

(40) Stanek, J.; Dziedzic-Kocurek, K. Magnetism of Ferriprotoporphyrin IX Monomers and Dimers. *J. Magn. Magn. Mater.* **2010**, *322* (8), 999–1003.

(41) Ramirez, A. P.; Espinosa, G. P.; Cooper, A. S. Strong Frustration and Dilution-Enhanced Order in a Quasi-2D Spin Glass. *Phys. Rev. Lett.* **1990**, *64* (17), 2070–2073.

(42) Shand, P. M.; Rash, T.; Streicher, M.; Kidd, T. E.; Boyle, K. R.; Strauss, L. H. Coercivity and Exchange Bias of $Mn_{0.25}Ti_{1.1}S_2$ in the Cluster-Glass State. *Phys. Rev. B* **2010**, *82* (21), 214413.

(43) Mydosh, J. A. *Spin Glasses: An Experimental Introduction*; CRC Press, 1993.

(44) Kumar, A.; Senyshyn, A.; Pandey, D. Evidence for Cluster Spin Glass Phase with Precursor Short-Range Antiferromagnetic Correlations in the B-Site Disordered $Ca(Fe_{1/2}Nb_{1/2})O_3$ Perovskite. *Phys. Rev. B* **2019**, *99* (21), 214425.

(45) Huser, D.; Duyneveldt, A. J. van; Nieuwenhuys, G. J.; Mydosh, J. A. Phenomenological Model for the Frequency Dependence of the Susceptibility of Spin Glasses and Related Compounds. *J. Phys. C: Solid State Phys.* **1986**, *19* (19), 3697–3717.

(46) Kearins, P.; Solana-Madruga, E.; Ji, K.; Ritter, C.; Attfield, J. P. Cluster Spin Glass Formation in the Double Double Perovskite $CaMnFeTaO_6$. *J. Phys. Chem. C* **2021**, *125* (17), 9550–9555.

(47) Aruga Katori, H.; Ito, A. Experimental Study of the de Almeida-Thouless Line by Using Typical Ising Spin-Glass $Fe_xMn_{1-x}TiO_3$ with x = 0.41, 0.50, 0.55 and 0.57. *J. Phys. Soc. Jpn.* **1994**, *63* (8), 3122–3128.

(48) Kotliar, G.; Sompolinsky, H. Phase Transition in a Dzyaloshinsky-Moriya Spin-Glass. *Phys. Rev. Lett.* **1984**, *53* (18), 1751–1754.

(49) Kaul, S. N.; Srinath, S. Irreversibility Lines in the H- T Phase Diagram of Re-Entrant Amorphous Ferromagnets. *J. Phys.: Condens. Matter* **1998**, *10* (48), 11067.

(50) Bag, P.; Baral, P. R.; Nath, R. Cluster Spin-Glass Behavior and Memory Effect in $Cr_{0.5}Fe_{0.5}Ga$. *Phys. Rev. B* **2018**, *98* (14), 144436.

(51) Edwards, S. F.; Anderson, P. W. Theory of Spin Glasses. *J. Phys. F: Met. Phys.* **1975**, *5* (5), 965.

(52) Süllow, S.; Nieuwenhuys, G. J.; Menovsky, A. A.; Mydosh, J. A.; Mentink, S. A. M.; Mason, T. E.; Buyers, W. J. L. Spin Glass Behavior in URh_2Ge_2. *Phys. Rev. Lett.* **1997**, *78* (2), 354–357.

(53) Moessner, R. Magnets with Strong Geometric Frustration. *Can. J. Phys.* **2001**, *79* (11–12), 1283–1294.

(54) Omari, R.; Prejean, J. J.; Souletie, J. Critical Measurements in the Spin Glass CuMn. *J. Phys. France* **1983**, *44* (9), 1069–1083.

(55) Shaginyan, V. R.; Stephanovich, V. A.; Msezane, A. Z.; Japaridze, G. S.; Clark, J. W.; Amusia, M. Ya.; Kirichenko, E. V. Theoretical and Experimental Developments in Quantum Spin Liquid in Geometrically Frustrated Magnets: A Review. *J Mater Sci* **2020**, *55* (6), 2257–2290.

(56) Balents, L. Spin Liquids in Frustrated Magnets. *Nature* **2010**, *464* (7286), 199–208.

(57) Souletie, J.; Tholence, J. L. Critical Slowing down in Spin Glasses and Other Glasses: Fulcher versus Power Law. *Phys. Rev. B* **1985**, *32* (1), 516–519.

(58) Bag, P.; Somesh, K.; Nath, R. A Study of Cluster Spin-Glass Behaviour at the Critical Composition $Mn_{0.73}Fe_{0.27}NiGe$. *J. Magn. Magn. Mater.* **2020**, *497*, 165977.

(59) Ogielski, A. T. Dynamics of Three-Dimensional Ising Spin Glasses in Thermal Equilibrium. *Phys. Rev. B* **1985**, *32* (11), 7384–7398.

(60) Pakhira, S.; Mazumdar, C.; Ranganathan, R.; Giri, S.; Avdeev, M. Large Magnetic Cooling Power Involving Frustrated Antiferromagnetic Spin-Glass State in R_2NiSi_3(R=Gd,Er). *Phys. Rev. B* **2016**, *94* (10), 104414.

(61) Lederman, M.; Orbach, R.; Hammann, J. M.; Ocio, M.; Vincent, E. Dynamics in Spin Glasses. *Phys. Rev. B* **1991**, *44* (14), 7403–7412.

(62) Lefloch, F.; Hammann, J.; Ocio, M.; Vincent, E. Can Aging Phenomena Discriminate Between the Droplet Model and a Hierarchical Description in Spin Glasses? *EPL* **1992**, *18* (7), 647.

(63) Katzgraber, H. G.; Palassini, M.; Young, A. P. Monte Carlo Simulations of Spin Glasses at Low Temperatures. *Phys. Rev. B* **2001**, *63* (18), 184422.

(64) Kirkpatrick, S.; Sherrington, D. Infinite-Ranged Models of Spin-Glasses. *Phys. Rev. B* **1978**, *17* (11), 4384–4403.

(65) Swendsen, R. H.; Wang, J.-S. Replica Monte Carlo Simulation of Spin-Glasses. *Phys. Rev. Lett.* **1986**, *57* (21), 2607–2609.

(66) Jayaprakash, C.; Chalupa, J.; Wortis, M. Spin-Glass Behavior from Migdal's Recursion Relations. *Phys. Rev. B* **1977**, *15* (3), 1495–1501.

(67) Schrenk, K. J.; Araújo, N. A. M.; Herrmann, H. J. Stacked Triangular Lattice: Percolation Properties. *Phys. Rev. E* **2013**, *87* (3), 032123.

(68) Southern, B. W.; Young, A. P.; Pfeuty, P. Effects of Percolation on Spin Glass Order. *J. Phys. C: Solid State Phys.* **1979**, *12* (4), 683.

(69) Marinari, E.; Parisi, G. Simulated Tempering: A New Monte Carlo Scheme. *EPL* **1992**, *19* (6), 451.

(70) Parisi, G. Order Parameter for Spin-Glasses. *Phys. Rev. Lett.* **1983**, *50* (24), 1946–1948.

(71) Maiolo, F.; Testaferri, L.; Tiecco, M.; Tingoli, M. Fragmentation of Aryl Alkyl Sulfides. A Simple, One-Pot Synthesis of Polymercaptobenzenes from Polychlorobenzenes. *J. Org. Chem.* **1981**, *46* (15), 3070–3073.

(72) Pijper, T. C.; Robertus, J.; Browne, W. R.; Feringa, B. L. Mild Ti-Mediated Transformation of t-Butyl Thio-Ethers into Thio-Acetates. *Org. Biomol. Chem.* **2014**, *13* (1), 265–268.

(73) Umemoto, T.; Garrick, L. M.; Saito, N. Discovery of Practical Production Processes for Arylsulfur Pentafluorides and Their Higher Homologues, Bis- and Tris(Sulfur Pentafluorides): Beginning of a New Era of "Super-Trifluoromethyl" Arene Chemistry and Its Industry. *Beilstein J. Org. Chem.* **2012**, *8* (1), 461–471.

(74) Pollak, J.; Tucaković, R. Über symmetrische Trithiophenole. *Monatshefte für Chemie* **1910**, *31* (7), 695–707.

Table of Contents Graphic: